

NONLINEAR MAGNETOINDUCTIVE TRANSMISSION LINES

NIKOS LAZARIDES[†], VASSILIS PALTOGLOU[‡] and G. P. TSIRONIS^{*}

*Department of Physics, University of Crete, and FORTH
P.O. Box 2208, 710 03, Heraklion, Crete, Greece*

[†]*nl@physics.uoc.gr*

[‡]*vaspal@physics.uoc.gr*

^{*}*gts@physics.uoc.gr*

Power transmission in one-dimensional nonlinear magnetic metamaterials driven at one end is investigated numerically and analytically in a wide frequency range. The nonlinear magnetic metamaterials are composed of varactor-loaded split-ring resonators which are coupled magnetically through their mutual inductances, forming thus a magnetoiductive transmission line. In the linear limit, significant power transmission along the array only appears for frequencies inside the linear magnetoiductive wave band. We present analytical, closed form solutions for the magnetoiductive waves transmitting the power in this regime, and their discrete frequency dispersion. When nonlinearity is important, more frequency bands with significant power transmission along the array may appear. In the equivalent circuit picture, the nonlinear magnetoiductive transmission line driven at one end by a relatively weak electromotive force, can be modeled by coupled resistive-inductive-capacitive (RLC) circuits with voltage-dependent capacitance. Extended numerical simulations reveal that power transmission along the array is also possible in other than the linear frequency bands, which are located close to the nonlinear resonances of a single nonlinear RLC circuit. Moreover, the effectiveness of power transmission for driving frequencies in the nonlinear bands is comparable to that in the linear band. Power transmission in the nonlinear bands occurs through the linear modes of the system, and it is closely related to the instability of a mode that is localized at the driven site.

PACS numbers:

Keywords: nonlinear split-ring resonators, magnetic metamaterials, driven linear waves, nonlinear power transmission

I. INTRODUCTION

The *metamaterial* concept usually refers to a periodic arrangement of artificially structured elements, designed to achieve advantageous and/or unusual electromagnetic properties compared to those of naturally occurring materials [42]. For example, the first metamaterial ever realized [40], exhibited negative refraction index in a narrow frequency band around 5 Gigahertz. The negative refraction index property requires that both the dielectric permittivity and the magnetic permeability are simultaneously negative. The most widely used elements for constructing a negative refractive index metamaterial are the electrically small resonant 'particles' called *split-ring resonators* (SRRs) and metallic wires. While the array of wires gives a negative permittivity below the plasma frequency, the array of the SRRs gives a negative magnetic permeability above their resonance frequency. Thus, the refraction index can be negative in a narrow frequency band. Since their discovery, metamaterials have been the target of intensive study. Although the development of metamaterials at microwave frequencies has progressed to the point where scientists and engineers are now pursuing applications, research on metamaterials that operate at higher frequencies is still in an early stage [25, 26, 43].

There is a wide subclass of metamaterials, that exhibit significant magnetic properties and even negative magnetic permeability at Terahertz and optical frequencies [13, 25, 51], even though they are made of non-magnetic

materials. Magnetism at such high frequencies is particularly important for the implementation of devices such as tunable lenses, adaptive mirrors, etc., since there are only a few natural materials that respond magnetically above microwaves. Moreover, magnetism in those natural materials is usually weak and within narrow frequency bands, limiting thus their use in possible Terahertz devices. The most common realization of such a *magnetic metamaterial* is composed of periodically arranged SRRs in a one- or two-dimensional lattices. In its simplest version an SRR is just a highly conducting [5, 13, 24] or superconducting [8] ring with a slit. The SRR structure was originally proposed by Pendry [30], who theoretically predicted that a periodic SRR-based structure could exhibit a negative magnetic permeability frequency band when irradiated by an alternating electromagnetic field of appropriate polarization. Pendry also realized that the SRR structure has considerable potential for enhancing nonlinear phenomena. When the SRR dimensions are much smaller than the wavelength of the incident field, the SRR can be regarded as an electric circuit consisting of inductive, capacitive and ohmic elements connected in series. The ring forms the inductance L , while the slit can be considered as a capacitor of capacitance C . The ohmic element R may represent all possible losses of the structure.

The next step was naturally to build nonlinearity in the SRR structure. Nonlinearity implies real-time tunability and multistability that is certainly a desired property of

possible future devices. The SRRs can become nonlinear either by the insertion of a strongly nonlinear dielectric [9] or a nonlinear electronic component (i.e., a varactor) [33, 34, 50] into their slits. Both ways would lead to effectively field dependent magnetic permeability for an array of nonlinear SRRs. Recently, the dynamic tunability by an external field for a two-dimensional array of varactor-loaded SRRs was demonstrated experimentally [37]. The SRRs in such an array are coupled through magnetic and/or electric dipole-dipole interactions, whose strength depends on the relative orientation of the SRRs and their slits in the array [6, 10, 31, 45].

In the equivalent circuit picture, the dynamics of a periodic nonlinear SRR array irradiated by an electromagnetic field, can be described by a set of coupled and driven ordinary differential equations with on-site nonlinearity. The discreteness, which is inherent in those SRR-based magnetic metamaterials, along with the nonlinearity and the weak coupling between their elements, allow for the generation of nonlinear excitations in the form of intrinsic localized modes or *discrete breathers* [41]. These nonlinear modes appear generically in discrete and nonlinear extended systems. Recent theoretical work in one- and two-dimensional nonlinear SRR lattices have demonstrated the existence and the stability of discrete breathers both in energy-conserving and dissipative systems [3, 4, 16, 18]. It has also demonstrated that breathers may be formed spontaneously through modulational instability in binary nonlinear magnetic metamaterials [20, 22, 29]. Moreover, domain-wall excitations [35] and envelope solitons [1, 2, 14, 48] may as well be excited in those systems, which seem to be stable even in the presence of noise [49].

The SRR-based magnetic metamaterials support a new kind of electromagnetic waves, the magnetoinductive waves, which exhibit phonon-like dispersion curves, and they can transfer energy along the array [39, 46, 47]. It is thus possible to fabricate a contact-free data and power transfer device, a *magnetoinductive transmission line*, which make use of the unique properties of the magnetic metamaterial structure, and may function as a frequency-selective communication channel for devices via their magneto-inductive wave modes [44]. In the present work we investigate the power transmission along a one-dimensional varactor-loaded SRR-based magnetic metamaterial, in the two possible geometries, which is driven at one end by a sinusoidal power source. In the linear limit, energy transfer along the array occurs only for driving frequencies in the linear magnetoinductive wave band. However, the nonlinearity could generate more frequency bands where efficient power transmission along the array is possible. Power transmission in chains of coupled anharmonic oscillators for driving frequencies in the band gap of the linear spectrum has been recently investigated, and that effect is referred to as self-induced transparency [28] or supratransmission [7]. For frequencies inside the linear magnetoinductive wave band the power is transmitted along the array from the magne-

toinductive wave modes, slightly modified by the presence of nonlinearity. However, for frequencies in the passbands resulting from nonlinearity, the power is transmitted along the array from nonlinear, breather-like excitations. In the next Section we derive the model equations for a varactor-loaded SRR-based magnetic metamaterial, where the nonlinearity has the form a polynomial expansion on the main variable, like that investigated in [50]. We also present bifurcation diagrams for the shortest possible end-driven array, i.e., an array with only two varactor-loaded SRRs, from which only one is directly driven. In Section III we obtain analytical solutions for the linear magnetoinductive waves of the end-driven, finite SRR array when losses are neglected, along with their discrete dispersion relation. In Section IV we present numerical results for power transmission and discuss their dependence on the model parameters for a short, end-driven varactor-loaded SRR array with and without an absorbing boundary at the non-driven end. We finish with concluding remarks in Section V.

II. VARACTOR-LOADED SRR ARRAY MODEL

Consider a ring-shaped or a squared split-ring resonator with a hyperabrupt tuning varactor mounted onto its slit. The varactor type could be selected from a large variety of available varactors, according to the needs of the experiment. In recent experimental works on varactor-loaded SRR-based metamaterials [11, 15, 32, 50], the varactor selected was a Skyworks SMV1231-079, whose voltage-dependent capacitance $C(U_D)$ (U_D is the voltage across the diode) is given by

$$C(U_D) = C_0 \left(1 - \frac{U_D}{U_p}\right)^{-M}, \quad (1)$$

where C_0 is the DC rest capacitance, U_p is the intrinsic potential, and M is a parameter. The values of those parameters are provided by the manufacturer SPICE model for that varactor to be

$$M = 0.8, \quad C_0 = 2.2 \text{ pF}, \quad U_p = 1.5 \text{ V}. \quad (2)$$

From Eq. (1) we can determine the voltage-dependence of the normalized charge

$$q = \frac{Q_D}{C_0 U_p}, \quad (3)$$

with Q_D being the charge in the diode, as a function of the normalized diode voltage $u = U_D/U_p$ as

$$q = \frac{1}{-M+1} \left[1 - (1-u)^{-M+1}\right]. \quad (4)$$

Assuming that $U_D < U_p$, the earlier equation can be solved for the diode voltage as a function of the charge, i.e., $u = u(q)$

$$u = 1 - [1 - q(-M+1)]^{\frac{1}{(-M+1)}}. \quad (5)$$

When $|x| \equiv |q(-M+1)| \ll 1$, the voltage u in the earlier equation can be expanded in a Taylor series in powers of q around zero. Thus, neglecting term of order $\mathcal{O}(q^4)$ or higher, we get

$$u = q + \alpha q^2 + \beta q^3, \quad (6)$$

where, by using Eq. (2),

$$\alpha = -\frac{M}{2} = -0.4, \quad \beta = \frac{1}{6}M(2M-1) = +0.08. \quad (7)$$

The expression Eq. (6) can then be used in the voltage equation, obtained from Kirchhoff's voltage law, which represents the varactor-loaded SRR as an effective resistive-inductive-capacitive (RLC) circuit with voltage-dependent capacitance

$$L \frac{d^2 Q_D}{dt^2} + R \frac{dQ_D}{dt} + U_p u = \mathcal{E}(t), \quad (8)$$

where

$$U_p u \equiv U_D = U_p \left[\frac{Q_D}{C_0 U_p} + \alpha \left(\frac{Q_D}{C_0 U_p} \right)^2 + \beta \left(\frac{Q_D}{C_0 U_p} \right)^3 \right], \quad (9)$$

, $\mathcal{E}(t)$ is the induced electromotive force of amplitude \mathcal{E}_0 and frequency ω resulting from an applied electromagnetic field with the same frequency, of the form

$$\mathcal{E}(t) = \mathcal{E}_0 \sin(\omega t), \quad (10)$$

where L is the inductance of the ring, R is the sum of the Ohmic resistance of the SRR ring and the series resistance of the diode, and t the temporal variable. The eigenfrequency ω_0 of the circuit described by Eq. (8) is given, in the linear limit without losses and driving, by

$$\omega_0 = \frac{1}{\sqrt{LC_0}}. \quad (11)$$

That approximate model of the varactor-loaded SRR is found to be adequate for varactor voltages not exceeding 0.5 V ($u \leq 1/3$ in normalized units), when the dissipative current of the varactor can be neglected [50].

Using Eq. (3) and the relations

$$\tau = t\omega_0, \quad \Omega = \frac{\omega}{\omega_0}, \quad \varepsilon_0 = \frac{\mathcal{E}_0}{U_p}, \quad (12)$$

Eq. (8) can be written in the normalized form

$$\begin{aligned} \frac{d^2 q}{d\tau^2} + q + \alpha q^2 + \beta q^3 + \gamma \frac{dq}{d\tau} \\ = \varepsilon_0 \sin(\Omega\tau), \end{aligned} \quad (13)$$

where

$$\gamma = R\sqrt{C_0/L} \quad (14)$$

is the normalized loss coefficient. The varactor-loaded SRR is a nonlinear oscillator, which exhibits multistability, hysteretic effects, and secondary resonances, when

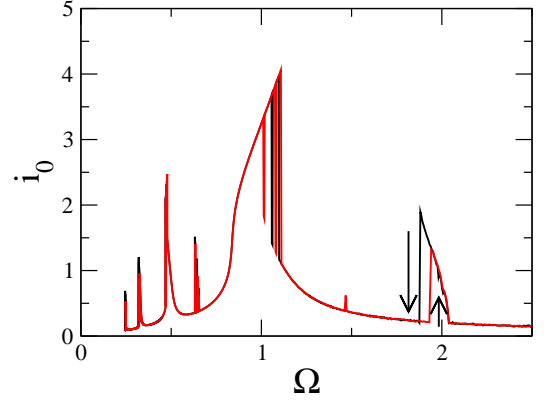


FIG. 1: The current amplitude i_0 as a function of the normalized frequency Ω for a varactor-loaded SRR modeled by Eq. (13). Red curve: frequency increases; black curve: frequency decreases.

driven by a sufficiently strong external field. A typical current amplitude i_0 - frequency Ω curve for the equivalent circuit model Eq. (13), like that shown in Fig. 1, exhibits all those characteristics. Notice the hysteresis loop at normalized frequency Ω around 1.1, close to the resonance frequency of the linear system, and the very strong resonance at its second harmonic, i.e., at $\Omega \simeq 2$, where a smaller hysteresis loop also appears. Furthermore, we observe a subharmonic resonance at $\Omega \simeq 0.48$, as well as weaker resonances at $\Omega \sim 0.63$, 0.33 and $\Omega \sim 0.25$. For frequency intervals lying between the boundaries of the hysteresis loops there are two different states of the oscillator, with low and high current amplitude, which are simultaneously stable.

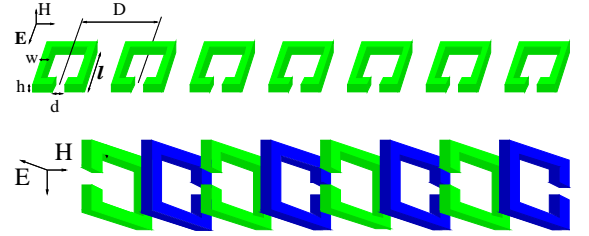


FIG. 2: Schematic of an SRR array in the planar geometry (upper) and in the axial geometry (lower).

Consider a one-dimensional periodic array of *identical* varactor-loaded SRRs, which are coupled magnetically to their first neighbors through their mutual inductances. The array can be formed in two possible geometries, according to the relative orientation of its elementary units (i.e., the SRRs) in the array. As can be seen in Fig. 2, the SRRs can be arranged either in the planar geometry, where all of them are lying on the same plane, or in the axial geometry, where the axes of all the SRRs are lying on the same line. The orientation of the incident electromagnetic field, which is also shown in the figure, is such that the magnetic component can excite an electromotive force in each SRR. Below we consider arrays that

are driven only at one end (let us say the left end). Thus only one SRR receives energy directly from the driver. However, the energy can be transmitted along the array due to the interaction between its elements. Including the coupling of each SRR to its nearest neighbors, we get for the charge $Q_{D,n}$ of the n -th varactor the dynamic equations

$$L \frac{dI_n}{dt} + RI_n + U_p u_n + M \frac{dI_{n-1}}{dt} + M \frac{dI_{n+1}}{dt} = \mathcal{E} \delta_{n,1} \quad (15)$$

where $n = 1, \dots, N$, with N being the total number of SRRs in the array, $I_n(t) = dQ_{D,n}/dt$ is the current flowing in the n -th SRR, $U_p u_n$ is the approximate voltage across the n -th varactor, and M (not to be confused with the varactor parameter) is the mutual inductance between two neighboring SRRs. Using the relations from Eq. (12), the coupled nonlinear Eqs. (15) can be written in normalized form as

$$\begin{aligned} \frac{d^2}{d\tau^2} (\lambda q_{n-1} + q_n + \lambda q_{n+1}) + q_n + \alpha q_n^2 + \beta q_n^3 = \\ -\gamma \frac{dq_n}{d\tau} + \varepsilon_0 \sin(\Omega\tau) \delta_{n,1}, \end{aligned} \quad (16)$$

where $\lambda = M/L$ is the coupling coefficient between neighboring SRRs. The function $\delta_{n,1}$ is unity for $n = 1$, while it is zero for any other n . The coupling parameter λ may assume both positive and negative values, corresponding to planar and axial geometry of the varactor-loaded SRR array, respectively.

For a particular array, the values of the coupling and loss coefficients λ and γ , respectively, can be estimated from its geometrical and material parameters. Specifically, the mutual inductance M , the ring inductance L , and the Ohmic resistance R_{SRR} of the ring can be calculated from the following expressions

$$M = \mu_0 \frac{\pi a^2 a^2}{4D^3}, \quad (17)$$

$$L = \mu_0 a \left[\ln \left(\frac{16a}{h} \right) - 1.75 \right], \quad (18)$$

$$R_{SRR} = \frac{2a}{\sigma h \delta}, \quad (19)$$

where μ_0 is the magnetic permeability in vacuum, a is the average radius of each SRR, h the diameter of the wire of each SRR, D is the center to center distance between neighboring SRRs, and σ and δ is the conductivity and skin depth of the SRR wire. Eqs. (17)–(19) refer to circular SRRs with circular cross-section. However, they can also be used for circular SRRs with square cross-section by defining an equivalent diameter of the SRR wire $h = \sqrt{4dw/\pi}$, with d and w being the depth and width, respectively, of the SRR wire. For $a \simeq 3.7$ mm, $D \simeq 11$ mm, $h \simeq 0.5$ mm, we get from Eqs. (17) and (18), respectively, that $M \simeq 0.14$ nH and $L \simeq 14$ nH, and consequently $\lambda \simeq 0.01$. For $\delta \simeq 2.2 \times 10^{-3}$ mm and $\sigma \simeq 0.5 \times 10^6$ (Ωcm) $^{-1}$ (for an SRR made of copper wire at ~ 1 GHz at room temperature) we get from Eq.

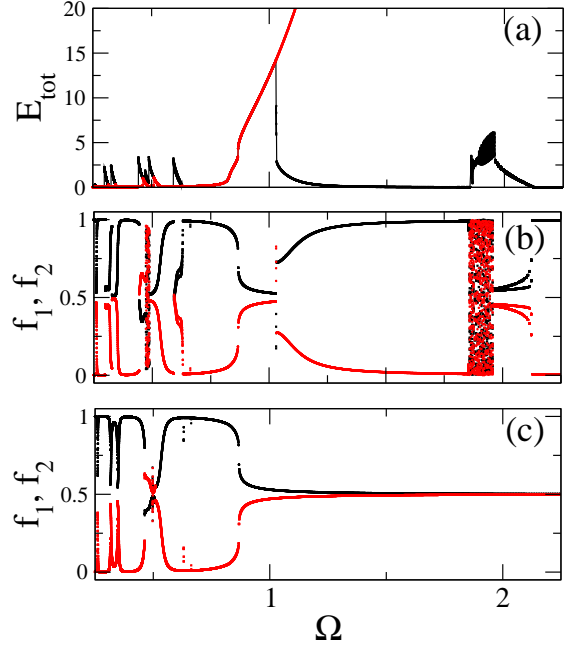


FIG. 3: (a) Energy E_{tot} bifurcation diagram for varying frequency Ω for an asymmetrically driven varactor-loaded SRR dimer with $\gamma = 0.001$, $\varepsilon_0 = 0.3$, and $\lambda = +0.01$. (b) Energy fractions f_1 and f_2 of the first (driven) and the second SRR, respectively, of the dimer in the low energy state. (c) Energy fractions f_1 and f_2 of the first (driven) and the second SRR, respectively, of the dimer in the high energy state.

(19) that $R_{SRR} \simeq 0.13$ Ω . The diode series resistance R_s of the varactor used in Ref. [50] is around $\simeq 2$ Ω ; that is, most of the Ohmic resistance of the varactor-loaded SRR, $R = R_{SRR} + R_s = 0.13 + 2.00 = 2.13$ Ω comes from the varactor. By substituting $R \simeq 2.13$ Ω in the second of Eq. (14), along with $L = 14$ nH and $C_0 = 2.2$ pF, we get that $\gamma = 0.027$. The resonance frequency of a single varactor-loaded SRR is $f_0 \simeq (2\pi\sqrt{LC_0})^{-1} \simeq 0.9$ GHz. In the numerical calculations below we used the estimated value of λ that indicates weakly coupled SRRs. However, we use a smaller value of γ , which could be achieved in practice by using a metallic wire with higher conductivity and an ultra-low resistance varactor with similar capacitance-voltage relation.

The shortest end-driven varactor-loaded SRR array is that comprised of two elements. Since only one of them is driven by the external field, we refer to this system as the asymmetrically driven nonlinear dimer. The increase of degrees of freedom leads to interesting and complicated behavior, that is marked by the appearance of chaos. In Fig. 3, the bifurcation diagram of the total energy E_{tot} of the dimer with varying normalized frequency Ω is shown for positive coupling λ . For negative coupling λ with equal strength we get very similar results that share a number of characteristic features. First of all, multistability is again present, for normalized frequencies in an interval around $\Omega \sim 0.9$. There, two simultaneously stable energy states, with high and low energy, co-exist, as it

is shown in Fig. 3a. The energy difference between those states increases considerably with increasing frequency. Moreover, low energy state becomes chaotic for frequencies around $\Omega \sim 1.9$. It is also interesting to see how the total energy is divided between the two elements. The energy fractions $f_1 = E_1/E_{tot}$ and $f_2 = E_2/E_{tot}$, with E_1 and E_2 being the energies of the first (driven) and second SRR of the dimer, are shown both for the high and the low energy states in Fig. 3b and 3c as a function of the normalized frequency Ω . When the dimer is in the low energy state, most of the energy is concentrated in driven SRR whose energy fraction is close to unity (correspondingly, the energy fraction of the other SRR is close to zero). However, for frequencies around the resonances, energy can be transferred easily from the one SRR to the other, and then the energy fractions of the SRRs in the dimer attain comparable values. In the chaotic regions, the energy is transferred irregularly from one SRR to the other and the energy fractions span the whole interval between zero and one. In the high energy state (Fig. 3c), the energy fractions are almost equal for frequencies above the linear resonance frequency, $\Omega \sim 1$. Below that frequency, the energy is either concentrated in the driven SRR (for frequencies far from resonances), or the values of the energy fractions are comparable (close to resonances).

III. DRIVEN LINEAR SOLUTIONS

For a weakly driven array, the nonlinear terms which are proportional to α and β are not so important and they can be neglected. Then, the system of Eqs. (16) reduces to a linear one

$$\begin{aligned} \frac{d^2}{d\tau^2} (\lambda q_{n-1} - q_n + \lambda q_{n+1}) + q_n \\ = -\gamma \frac{dq_n}{d\tau} + \varepsilon_0 \sin(\Omega\tau) \delta_{n,1}. \end{aligned} \quad (20)$$

The dispersion relation of the linear system can be obtained by the substitution $q_n = A \cos(\kappa n - \Omega\tau)$ in the absence of losses and applied field, i.e., for $\varepsilon_0 = 0$ and $\gamma = 0$, which gives the linear dispersion of magnetoiductive waves

$$\Omega_\kappa = \frac{1}{\sqrt{1 + 2\lambda \cos(\kappa)}}, \quad (21)$$

where κ is the (normalized) wavevector ($-\pi \leq \kappa \leq \pi$). Eq. (21) defines a frequency band of width $\Delta\Omega \simeq 2\lambda$ that is bounded by a minimum and a maximum frequency $\Omega_{min} = 1/\sqrt{1 + 2\lambda}$ and $\Omega_{max} = 1/\sqrt{1 - 2\lambda}$, respectively.

However, it is also possible to calculate the dispersion, expressed as a series of resonant frequencies, and the exact form of the linear magnetoiductive modes for the finite system in the absence of losses ($\gamma = 0$). For finite systems, Eq. (20) should be implemented with free-end boundary conditions, to account for the termination of

the structure, i.e.,

$$q_0 = q_{N+1} = 0. \quad (22)$$

By substituting $q_n = Q_n \sin(\Omega\tau)$ into Eq. (20), the stationary equations can be written as

$$sQ_{n-1} + Q_n + sQ_{n+1} = \kappa, \quad (23)$$

where

$$s = -\frac{\lambda\Omega^2}{1 - \Omega^2}, \quad \kappa = \frac{\varepsilon_0}{1 - \Omega^2} \delta_{n,1}, \quad (24)$$

or, in matrix form

$$\mathbf{Q} = \kappa \hat{\mathbf{S}}^{-1} \mathbf{E}_1, \quad (25)$$

where \mathbf{Q} and \mathbf{E}_1 are N -dimensional vectors with components Q_i and $\delta_{i,1}$, respectively, and $\hat{\mathbf{S}}^{-1}$ is the inverse of the $N \times N$ coupling matrix $\hat{\mathbf{S}}$. The latter is a real, symmetric tridiagonal matrix that has diagonal elements equal to unity, while all the other non-zero elements are equal to s . The need to find the inverse of tridiagonal matrices like $\hat{\mathbf{S}}$ arises in many scientific and engineering applications. Recently, Huang and McColl [12] related the inversion of a general tridiagonal matrix to second order linear recurrences, and they provided a set of very simple analytical formulae for the elements of the inverse matrix. Those formulae lead immediately to closed forms for certain tridiagonal matrices, like $\hat{\mathbf{S}}$ [21]. The components of the \mathbf{Q} vector can be written as

$$Q_i = \kappa \left(\hat{\mathbf{S}}^{-1} \right)_{i1}, \quad (26)$$

where $\left(\hat{\mathbf{S}}^{-1} \right)_{i1}$ is the $(i1)$ -element of the inverse coupling matrix $\hat{\mathbf{S}}^{-1}$, whose explicit form is given in [21]. Then, the solution of the linear system Eq. (20) and (22) for any driving frequency and finite N is given by

$$\begin{aligned} q_n(\tau) = \kappa\mu \frac{\sin[(N-n+1)\theta']}{\sin[(N+1)\theta']} \sin(\Omega\tau), \\ \theta' = \cos^{-1} \left(\frac{1}{2|s|} \right), \end{aligned} \quad (27)$$

for $s > +1/2$ and $s < -1/2$, and

$$\begin{aligned} q_n(\tau) = \kappa\mu \frac{\sinh[(N-n+1)\theta]}{\sinh[(N+1)\theta]} \sin(\Omega\tau), \\ \theta = \ln \frac{1 + \sqrt{1 - (2s)^2}}{2|s|}, \end{aligned} \quad (28)$$

for $-1/2 < s < +1/2$, where

$$\mu = \frac{1}{|s|} \left(-\frac{|s|}{s} \right)^{n-1}. \quad (29)$$

Note that the Q_i s are uniquely determined by the parameters of the system.

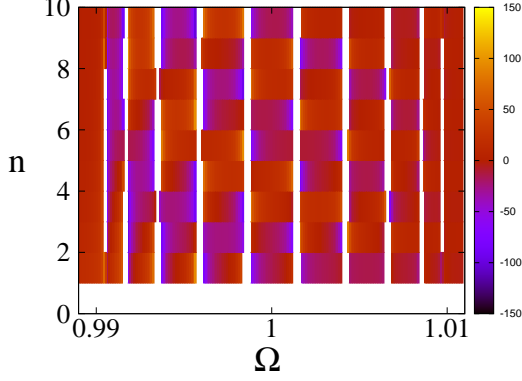


FIG. 4: Density plots of the Q_n 's in a stationary state, on the site number n - normalized frequency Ω plane calculated from the analytical expressions Eqs. (27) and (28) for $\lambda = +0.01$ and $\varepsilon_0 = 0.3$. The vertical white bands indicate the positions of the resonances.

From the analytical solution in the linear magnetoinductive wave band, Eq. (27), which corresponds to either $s > +1/2$ or $s < -1/2$, we can infer the resonant frequencies from zeroing the denominator, i.e., by setting $\sin[(N+1)\theta'] = 0$. Then we see that the solution has a resonance for

$$s \equiv s_m = \frac{1}{2 \cos \left[\frac{m\pi}{(N+1)} \right]}, \quad (30)$$

where m is an integer ($m = 1, \dots, N$). The resonant frequencies are obtained by solving the first of Eq. (24) with respect to Ω , and substituting the resonant values of $s \equiv s_m$ from Eq. (30). Then we get the discrete dynamic dispersion relation of linear magnetoinductive waves in the varactor-loaded SRR array, the discrete analogue of Eq. (21), as

$$\Omega_m = \frac{1}{\sqrt{1 - 2\lambda \cos \left(\frac{m\pi}{N+1} \right)}}, \quad (31)$$

where m is the mode number ($m = 1, \dots, N$). In Fig. 4, a density plot of the Q_n 's on the n - Ω plane, calculated analytically from Eqs. (27) and (28), is shown for positive coupling coefficient λ . In the frequency interval shown, the Q_n 's have rather large values because, due to the narrow band, all frequencies are very close to a resonance. Moreover, the analytical solutions presented above have been obtained in the absence of losses, so that there is nothing to prevent the Q_n 's from increasing indefinitely close to a resonance (and to go to infinity exactly at resonance). The white vertical regions in these figures correspond to frequency intervals around a resonance, where the Q_n 's have very large values. Thus, those regions indicate the frequencies of the resonances. We can also

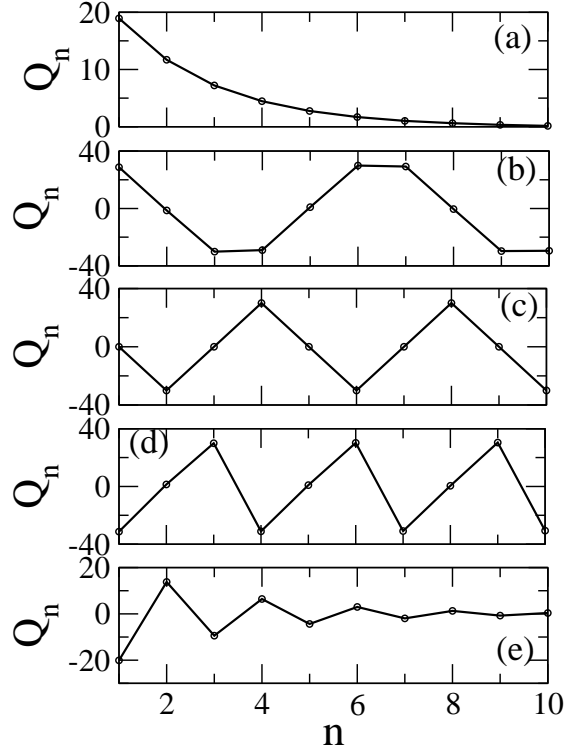


FIG. 5: Typical profiles calculated analytically from Eqs. (27) and (28) for $\lambda = +0.01$, $\varepsilon_0 = 0.3$, and five different frequencies: (a) $\Omega = 0.989$; (b) $\Omega = 0.995$; (c) $\Omega = 1.000$; (d) $\Omega = 1.005$; (e) $\Omega = 1.011$. The frequencies in (a) and (e) lie outside the linear magnetoinductive wave band.

see in Fig. 4 that the solutions close to the lower bound ($\Omega_{min} \simeq 0.99$) of the linear magnetoinductive wave band exhibit very high amplitudes. For negative coupling coefficient with equal strength the high amplitude solutions appear close to the upper bound ($\Omega_{max} \simeq 1.01$) of the linear magnetoinductive wave band.

In Fig. 5 the profiles of the analytical solutions for five different frequencies, both inside and outside the linear magnetoinductive wave band are shown for positive λ . The frequencies in Figs. 5a and 5e lie outside the linear band, so that the Q_n 's decrease exponentially with increasing site number n .

IV. POWER TRANSMISSION ALONG THE ARRAY.

In the following we focus on the power transmission along a varactor-loaded SRR array with $N = 10$ elements, which is driven at the left end ($n = 1$). The average power dissipated in the n -th SRR is defined as

$$P_n = R \langle I_n^2(\tau) \rangle_{\tau_0}, \quad (32)$$

where $\langle \rangle_{\tau_0}$ denotes time-average over τ_0 time-units. The power density P_n can be normalized to $P_0 = I_0^2 R$, where $I_0 = \omega_0 C_0 U_p$ and R the value of resistance that

results from the value of the dissipation coefficient used in the simulations. For $\gamma = 0.001$ we have that $R \simeq 0.06$ and $P_0 \simeq 28 \mu W$. It is convenient to express P_n in dBm, according to the relation

$$P_n(\text{dBm}) = 20 \log \left(\langle i_n^2 \rangle_{\tau_0} \frac{P_0(\text{in } W)}{1 \text{ mW}} \right) \simeq 4.34 \ln(0.028 \langle i_n^2 \rangle_{\tau_0}), \quad (33)$$

where i_n is the normalized current in the n -th SRR.

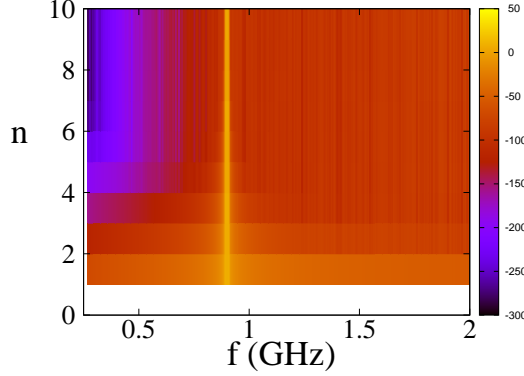


FIG. 6: Average power density plot (in dBm) on the $n - f$ plane, for $\lambda = +0.01$, $\gamma = 0.001$, and $\epsilon_0 = 0.3$, in the linear regime ($\alpha = 0$, $\beta = 0$).

The system of Eqs. (16) is integrated with a 4th order Runge-Kutta algorithm with fixed time-stepping, and boundary conditions $q_0 = q_{N+1} = 0$ to account for the termination of the structure. The initial conditions were set to zero. The time allowed for the elimination of transients in each value of the frequency is $2000 T_0$ ($T_0 = 2\pi/\omega_0$), while the time interval τ_0 over which the average power is calculated is typically $1000 T_0$. In order to convert time intervals to physical units one has to multiply by the inverse of the resonance frequency f_0^{-1} , which gives $\tau_0 \simeq 2.2 \mu s$. In the linear regime, i.e., $\alpha = 0$ and $\beta = 0$, the average power $P(\text{dBm})$ density plot on the site number n - frequency f plane shown in Fig. 6 exhibits the expected behavior; that appreciable power transmission only occurs for frequencies in the linear band, i.e., around $f = 0.9 \text{ GHz}$. However, the activation of the nonlinear terms reveals that even a relatively low driving amplitude $\epsilon_0 = 0.3$ is sufficient for nonlinear power transmission bands to be formed. Thus, power can be transmitted not only for frequencies in the linear band, but also in the otherwise forbidden frequency regions. As it can be observed in Fig. 7, a number of transmission bands have appeared due to the nonlinearity. The array thus becomes transparent in power transmission at frequency intervals around the nonlinear resonances of a single varactor-loaded SRR oscillator. That self-induced transparency is a robust effect and survives with considerably increased losses, as it is shown in Fig. 8, where

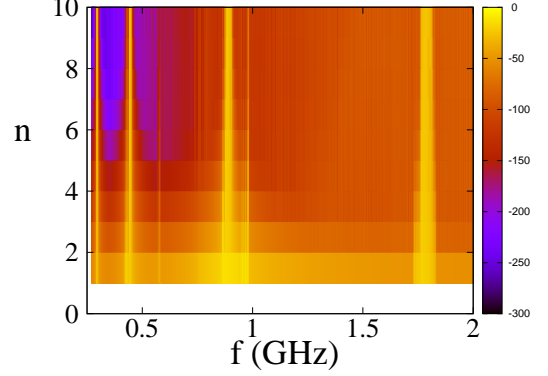


FIG. 7: Average power density plot (in dBm) on the $n - f$ plane, for $\lambda = +0.01$, $\gamma = 0.001$, $\alpha = -0.4$, $\beta = 0.08$, and $\epsilon_0 = 0.3$.

the loss coefficient has been increased by an order of magnitude (from 0.001 to 0.01). In the density plots shown above, significant power transmission is indicated by red color. In both Figs. 7 and 8, nonlinear power transmission occurs at $f \sim 0.3 \text{ GHz}$, $f \sim 0.45 \text{ GHz}$, and $f \sim 1.8 \text{ GHz}$. The latter nonlinear band, around the second harmonic of the resonance frequency of the linear system, seems to be the wider of all.

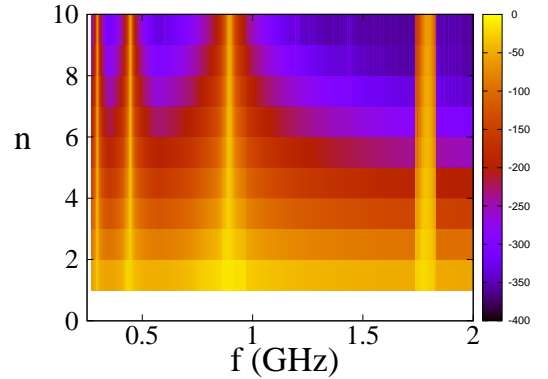


FIG. 8: Average power density plot (in dBm) on the $n - f$ plane, for $\lambda = +0.01$, $\gamma = 0.01$, $\alpha = -0.4$, $\beta = 0.08$, and $\epsilon_0 = 0.3$.

When losses are small, the appearance of more nonlinear bands is possible, like the one seen just above the linear band in Fig. 7, at $f \sim 1 \text{ GHz}$. That transmission band is due to an interplay between nonlinearity and geometrical (lattice) resonances, and it is very sensitive to changes in the parameters of the model. Note that in the density plots presented above the frequency is given in natural units, using the relation $f = f_0 \Omega = 0.9\Omega \text{ GHz}$.

It is very illuminating to see the time evolution of the current flowing in each SRR of the array for some frequencies in the transmission bands. We have chosen two different frequencies, one in the linear band and one the high frequency band which is around the second harmonic of the linear resonance frequency. The time evolution of the currents in the first, fourth, seventh, and tenth (last) SRR are shown for $f = 0.888 \text{ GHz}$ and $f = 1.78 \text{ GHz}$ in Figs. 9a and 9b, respectively. The currents oscillate periodically in all SRRs, although with different amplitudes and relative phases with respect to the driver. This figure suggests that power transmission for frequencies in the forbidden band gap occurs through the linear modes of the system. For frequencies outside the linear and nonlinear bands, the currents exhibit similar oscillations, although their amplitude becomes vanishingly small with increasing site number n . The relative efficiency of power transmission in the two

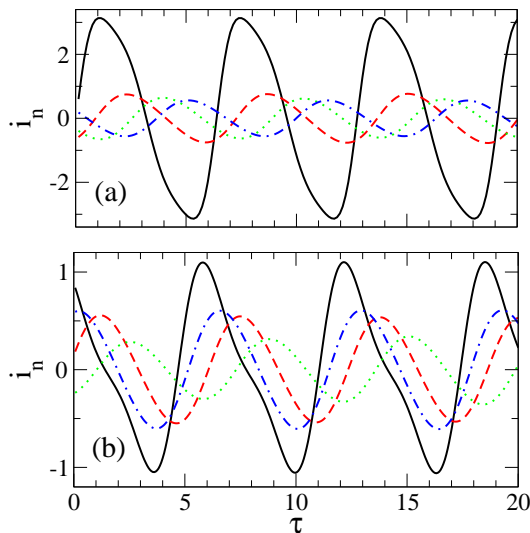


FIG. 9: Time dependence of the current i_n in the n -th SRR for an array with $N = 10$, $\lambda = 0.01$, $\epsilon_0 = 0.3$, $\gamma = 0.001$, and frequency (a) $f = 0.888 \text{ GHz}$; (b) $f = 1.78 \text{ GHz}$. The four different curves are for the current in the $n = 1$ SRR (black-solid), $n = 4$ SRR (red-dashed), $n = 7$ SRR (green-dotted), $n = 10$ SRR (blue-dot-dashed).

frequencies used in the previous figure, are shown in Fig. 10, along with the power transmission for a specific frequency ($f = 1.197 \text{ GHz}$) outside all linear and nonlinear bands. It is remarkable that the transmission efficiency is almost the same for frequencies in the two pass-bands, while for the other one the transmitted power practically vanishes at the fourth site.

In the density plots above, the right boundary was actually a reflecting one, allowing the formation of stationary states in the array. We have also used a totally absorbing boundary by adding five more sites at the right end of the array, where the damping coefficient increases exponentially with increasing site number. Thus, the waves coming from the left are completely damped at

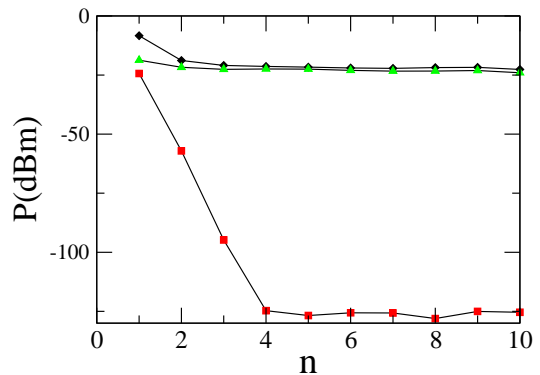


FIG. 10: Power transfer efficiency in different frequency regions, i.e., average power (in dBm) as a function of site number n for an array $\epsilon_0 = 0.3$, $\lambda = 0.01$, $\gamma = 0.001$, $N = 10$, and $f = 0.888 \text{ GHz}$ (black diamonds); $f = 1.197 \text{ GHz}$ (red squares), $f = 1.78 \text{ GHz}$ (green triangles).

the end of the extended array, and no reflection occurs. The total number of SRRs is now $N' = N + N_1$ where $N_1 = 5$, and the dissipation coefficient γ is now a function of the site number n , $\gamma(n)$, given by

$$\gamma(n) = \begin{cases} \gamma & , 1 \leq n \leq N \\ \gamma e^{\mu n} & , N < n \leq N' \end{cases} \quad (34)$$

where $\mu = \frac{\log(1/\gamma)}{N_1}$, with $\gamma = 0.001$ as before. For the array with n -dependent dissipation coefficient, a typical average power density plot is shown in Fig. 11, where the power in each site is the average over a time interval of $5000 T_0$. We observe, at least for the first N sites of the array, a pattern similar with those seen in Figs. 7 and 8. That is, the appearance of the linear and the nonlinear transmission bands at about the same frequency intervals. We also observe that almost all of the transmitted power is absorbed from the five last sites of the array. Importantly, the narrow band coming from geometrical resonances in Figs. 7 and 8, which is around $f = 1 \text{ GHz}$, appears in Fig. 11 as well, and moreover it seems that it is capable of transmitting power to the end of the array.

V. DISCUSSION AND CONCLUDING REMARKS

We have used a simple electric circuit model of inductively coupled resistive-inductive-capacitive circuits with voltage-dependent capacitance to investigate the transmission of power in a one-dimensional, end-driven, nonlinear magnetic metamaterial comprised of varactor-loaded SRRs. We have used both a reflecting and an absorbing boundary for the end that is not driven by the external field. The importance of such discrete models for describing the dynamic behaviour of SRR-based magnetic metamaterials has been recently appreciated [27],

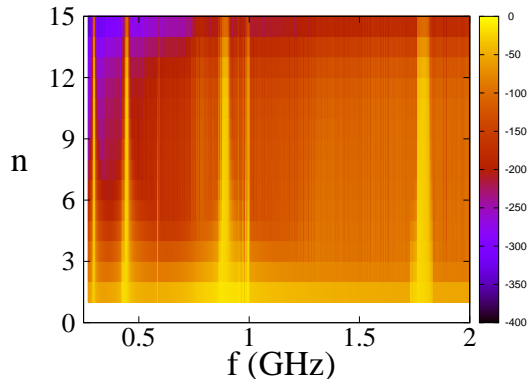


FIG. 11: Average power density plot P_n (in dBm) on the $n-f$ plane for a varactor-loaded SRR array with absorbing right boundary (see text), for $\lambda = +0.01$, $\epsilon_0 = 0.297$, $\gamma = 0.001$, and $N' = 15$ ($N = 10$).

although similar discrete models have been employed earlier for the study of localized excitations in those systems [16, 35]

In the present work, we have focused on the transmission of power along the array, and especially that in the nonlinear regime, which results in the formation of nonlinear pass-bands for frequencies close to the resonances of a single varactor-loaded SRR that is described by the approximate model equation (13). The approximate model holds fairly well for relatively low driving amplitudes, for which the dissipative diode current of the varactor can be neglected. It seems, thus that the properties of the individual elements of the array predominantly determine its transmission properties, at least in the case of weak magnetoinductive coupling investigated in the present work. The numerical results demonstrate that the nonlinear pass-bands transmit power with efficiently comparable to that of the linear band. For the parameter sets used in this work, which are close to those in [50] for a single varactor-loaded SRR, there are three nonlinear bands, both above and below the linear band.

Their width apparently depends on the frequency, i.e., the bands at higher frequencies are significantly wider than those at lower frequencies.

Moreover, we have also observed the formation, either complete or partial, of another nonlinear pass-band at frequencies slightly above the linear band (at $f \sim 1$ GHz). That band, which is rather narrow and can be observed both in Figs. 7 and 8 as well as in Fig. 11, seem to depend sensitively on the model parameters λ , f , ϵ_0 (for α and β fixed), and mainly on the loss coefficient γ . Comparing Figs. 7 and 8, which have been obtained for different loss coefficient $\gamma = 0.001$ and 0.01 , respectively, we see that the power transmission in that band considerably decreases when the losses increase by an order of magnitude. That type of nonlinear band appears due to geometrical resonances of the standing waves that are formed in the array due to driving at one end. Geometrical resonances seem to offer an important mechanism for the generation of nonlinear pass-bands, which can be employed for constructing transmission lines with banded power transmission spectra with bands at desired frequency ranges. Similar conduct-free transmission lines could be formed by superconducting magnetic metamaterials, where the basic structural element (the SRR) is replaced by its direct superconducting analogue, the rf SQUID [17, 19]. The rf SQUID, where the acronym stands for radio-frequency superconductive quantum interference device, is just a superconducting ring interrupted by a Josephson junction, which makes it an intrinsically nonlinear element. A one-dimensional array of rf SQUIDs coupled through their mutual inductances forms a nonlinear magnetoinductive transmission line [19] whose power transmission properties is a matter of future work.

Acknowledgments

This work was supported in part by the European Office of Aerospace Research and Development, AFSOR award FA8655-10-1-3039, and by the EURYI and MEXT-CT-2006-039047.

-
- [1] Cui, W., Zhu, Y.-Y., Li, H.-x. & Liu, S. [2009] “Self-induced gap solitons in nonlinear magnetic metamaterials,” *Phys. Rev. E* **80**, 036608-1–036608-5.
 - [2] Cui, W., Zhu, Y.-Y., Li, H.-X. & Liu, S. [2010] “Solitons excitations in a one-dimensional nonlinear diatomic chain of split-ring resonators,” *Phys. Rev. E* **81**, 016604-1–016604-9.
 - [3] Eleftheriou, M., Lazarides, N. & Tsironis, G. P. [2008] “Magnetoinductive breathers in metamaterials,” *Phys. Rev. E* **77**, 036608-1–036608-13.
 - [4] Eleftheriou, M., Lazarides, N., Tsironis, G. P. & Kivshar, Yu. S. [2009] “Surface magnetoinductive breathers in two-dimensional magnetic metamaterials,” *Phys. Rev. E* **80**, 017601-1–017601-4.
 - [5] Enkrich, C., [2005] “Magnetic metamaterials at telecommunication and visible frequencies,” *Phys. Rev. Lett.* **95**, 203901-1–203901-4.
 - [6] Feth, N., König, M., Husnik, M., Stannigel, K., Niegemann, J., Busch, K., Wegener, M. & Linden, S. [2010] “Electromagnetic interaction of split-ring resonators: The role of separation and relative orientation,” *Opt. Express* **18**, 6545–6554.
 - [7] Geniet, F. & Leon, J. [2002] “Energy transmission in the forbidden band gap of a nonlinear chain,” *Phys. Rev. Lett.*

- 89, 134102-1–134102-4.
- [8] Gu, J., Singh, R., Tian, Z., Cao, W., Xing, Q., He, M.-X., Zhang, J. W., Han, J., Chen, H. & Zhang, W. [2010] “Terahertz superconductor metamaterial,” *Appl. Phys. Lett.* **97**, 071102-1–071102-3.
 - [9] Hand, T. H. & Cummer, S. A. [2008] “Frequency tunable electromagnetic metamaterial using ferroelectric loaded split rings,” *J. Appl. Phys.* **103**, 066105-1–066105-3.
 - [10] Hesmer, F., Tatartschuk, E., Zhuromskyy, O., Radkovskaya, A. A., Shamonin, M., Hao, T., Stevens, C. J., Faulkner, G., Edwardds, D. J. & Shamonina, E. [2007] “Coupling mechanisms for split-ring resonators: Theory and experiment,” *Phys. Stat. Sol. (B)* **244**, 1170–1175.
 - [11] Huang, D., Poutrina, E. & Smith, D. R. [2010] “Analysis of the power dependent tuning of a varactor-loaded metamaterial at microwave frequencies,” *Appl. Phys. Lett.* **96**, 104104-1–104104-3.
 - [12] Huang, Y. & McColl, W. F. [1997] “Analytical inversion of general tridiagonal matrices,” *J. Phys. A: Math. Gen.* **30**, 7919–7933.
 - [13] Katsarakis, N., [2005] “Magnetic response of split-ring resonators in the far infrared frequency regime,” *Opt. Lett.* **30**, 1348–1350.
 - [14] Kourakis, I., Lazarides, N. & Tsironis, G. P. [2007] “Self-focusing and envelope pulse generation in nonlinear magnetic metamaterials,” *Phys. Rev. E* **75**, 067601-1–067601-4.
 - [15] Larouche, S., Rose, A., Poutrina, E., Huang, D. & Smith, D. R. [2010] “Experimental determination of the quadratic nonlinear magnetic susceptibility of a varactor-loaded split ring resonator metamaterial,” *Appl. Phys. Lett.* **97**, 011109-1–011109-3.
 - [16] Lazarides, N., Eleftheriou, M. & Tsironis, G. P. [2006] “Discrete breathers in nonlinear magnetic metamaterials,” *Phys. Rev. Lett.* **97**, 157406-1–157406-4.
 - [17] Lazarides, N. & Tsironis, G. P. [2007] “rf superconducting quantum interference device metamaterials,” *Appl. Phys. Lett.* **90**, 163501-1–163501-3.
 - [18] Lazarides, N., Tsironis, G. P. & Kivshar, Yu. S. [2008] “Surface breathers in discrete magnetic metamaterials,” *Phys. Rev. E* **77**, 065601(R)-1–065601(R)-4.
 - [19] Lazarides, N., Tsironis, G. P. & Eleftheriou, M. [2008] “Dissipative discrete breathers in rf SQUID metamaterials,” *Nonlin. Phen. Compl. Syst.* **11**, 250–258.
 - [20] Lazarides, N., Molina, M. I. & Tsironis, G. P. [2009] “Breather induction by modulational instability in binary metamaterials,” *Acta Phys. Pol. A* **116**, 635–637.
 - [21] Lazarides, N. & Tsironis, G. P. [2010] “Driven linear modes: Analytical solutions for finite discrete systems,” *Phys. Lett. A* **374**, 2179–2181.
 - [22] Lazarides, N., Molina, M. I. & Tsironis, G. P. [2010] “Breathers in one-dimensional binary metamaterial models,” *Physica B* **405**, 3007–3011.
 - [23] Lazarides, N., Molina, M. I., Tsironis, G. P. & Kivshar, Yu. S. [2010] “Multistability and localization in coupled nonlinear split-ring resonators,” *Phys. Lett. A* **374**, 2095–2097.
 - [24] Linden, S., Enkrich, C., Dolling, G., Klein, M. W., Zhou, J., Koschny, T., Soukoulis, C. M., Burger, S., Schmidt, F. & Wegener, M. [2004] “Magnetic response of metamaterials at 100 Terahertz,” *Science* **306**, 1351–1353.
 - [25] Linden, S., Enkrich, C., Dolling, G., Klein, M. W., Zhou, J., Koschny, T., Soukoulis, C. M., Burger, S., Schmidt, F. & Wegener, M. [2006] “Photonic metamaterials: magnetism at optical frequencies,” *IEEE J. Sel. Top. Quant. Electron.* **12**, 1097–1105.
 - [26] Litchinitser, N. M. & Shalaev, V. M. [2008] “Photonic metamaterials,” *Laser Phys. Lett.* **5**, 411–420.
 - [27] Liu, N., Liu, H., Zhu, S. N. & Giessen, H. [2009] “Stereometamaterials,” *Nature Photon.* **3**, 157– .
 - [28] Maniadis, P., Kopidakis, G. & Aubry, S. [2006] “Energy dissipation threshold and self-induced transparency in systems with discrete breathers,” *Physica D* **216**, 121–135.
 - [29] Molina, M. I., Lazarides, N. & Tsironis, G. P. [2009] “Bulk and surface magnetoinductive breathers in binary metamaterials,” *Phys. Rev. E* **80**, 046605-1–046605-9.
 - [30] Pendry, J. B., Holden, A. J., Robbins, D. J. & Stewart, W. J. [1999] “Magnetism from conductors and enhanced nonlinear phenomena,” *IEEE Trans. Microwave Theory Tech.* **47**, 2075–2084.
 - [31] Penciu, R. S., Aydin, K., Kafesaki, M., Koschny, Th., Ozbay, E., Economou, E. N. & soukoulis, C. M. [2008] “Multi-gap individual and coupled split-ring resonator structures,” *Opt. Express* **16**, 18131–18144.
 - [32] Poutrina, E., Huang, D. & Smith, D. R. [2010] “Analysis of nonlinear electromagnetic metamaterials,” *New J. Phys.* **12**, 093010-1–093010-27.
 - [33] Powell, D. A., Shadrivov, I. V., Kivshar, Yu. S. & Gorkunov, M. V. [2007] “Self-tuning mechanisms of nonlinear split-ring resonators,” *Appl. Phys. Lett.* **91**, 144107-1–144107-3.
 - [34] Shadrivov, I. V., Morrison, S. K. & Kivshar, Yu. S. [2006] “Tunable split-ring resonators for nonlinear negative-index metamaterials,” *Opt. Express* **14**, 9344–9349.
 - [35] Shadrivov, I. V., Zharov, A. A., Zharova, N. A. & Kivshar Yu. S. [2006] “Nonlinear magnetoinductive waves and domain walls in composite metamaterials,” *Photonics Nanostruct. Fundam. Appl.* **4**, 69–74.
 - [36] Shadrivov, I. V., Reznik, A. N. & Kivshar Yu. S. [2007] “Magnetoinductive waves in arrays of split-ring resonators,” *Physica B* **394**, 180–183.
 - [37] Shadrivov, I. V., Kozyrev, A. B., van der Weide, D. W. & Kivshar, Yu. S. [2008] “Tunable transmission and harmonic generation in nonlinear metamaterials,” *Appl. Phys. Lett.* **93**, 161903-1–161903-3.
 - [38] Shalaev, V.M. [2007] , “Optical negative-index metamaterials,” *Nature Photonics* **1**, 41–48.
 - [39] Shamonina, E. & Solymar, L. [2004] “Magneto-inductive waves supported by metamaterials elements: components for a one-dimensional waveguide,” *J. Phys. D: Appl. Phys.* **37**, 362– .
 - [40] Shelby, R. A., Smith, D. R. & Schultz, S. [2001] “Experimental verification of a negative index of refraction,” *Science* **292**, 77–79.
 - [41] Sievers, C. & Takeno, C. [1988] “Intrinsic localized modes in anharmonic crystals,” *Phys. Rev. Lett.* **61**, 970–973.
 - [42] Smith, D. R., Pendry, J. B. & Wiltshire, M. C. K. [2004] “Metamaterials and negative refractive index,” *Science* **305**, 788–792.
 - [43] Soukoulis, C. M., Linden, S. & Wegener, M. [2007] “Negative refractive index at optical wavelengths,” *Science* **315**, 47–49.
 - [44] Stevens, C. J., Chan, C. W. T., Stamatis, K. & Edwards, D. J. [2010] “Magnetic metamaterials as 1-D data transfer channels: An application for magneto-inductive waves,” *IEEE Trans. Microw. Theory Techniques* **58**, 1248–1256.
 - [45] Sydoruk, O., Radkovskaya, A., Zhuromskyy, O., Sha-

- monina, E., Shamonin, M., Stevens, C. J., Faulnker, G., Edwards, D. J. & Solymar, L. [2006] "Tailoring the near-field guiding properties of magnetic metamaterials with two resonant elements per unit cell," *Phys. Rev. B* **73**, 224406-1–224406-12.
- [46] Syms, R. R. A., Young, I. R. & Solymar, L. [2006] "Low-loss magneto-inductive waveguides," *J. Phys. D: Appl. Phys.* **39**, 3945– .
- [47] Syms, R. R. A., Solymar, L., Young, I. R. & Floume, T. [2010] "Thin-film magneto-inductive cables," *J. Phys. D: Appl. Phys.* **43**, 055102-1–055102-7.
- [48] Tsironis, G. P., Lazarides, N. & Eleftheriou, M. [2010] "Discrete breathers and solitons in metamaterials," *Springer Series in Optical Sciences* **150**, 273–285.
- [49] Tsurumi, T. [2008] "Soliton Propagation in Nonlinear Magnetic Metamaterials with Microscopic Disorder," *J. Phys. Soc. Jpn.* **77**, 074006-1–074006-8.
- [50] Wang, B., Zhou, J., Koschny, T. & Soukoulis C. M. [2008] "Nonlinear properties of split-ring resonators," *Opt. Express* **16**, 16058–16064.
- [51] Yen, T. J., Padilla, W. J., Fang, N., Vier, D. C., Smith, D. R., Pendry, J. B., Basov, D. N. & Zhang, X. [2004] "Terahertz magnetic response from artificial materials," *Science* **303**, 1494–1496.